

Strong 3D Printing by TPMS Injection

Xin Yan, Cong Rao, Lin Lu, Andrei Sharf, Haisen Zhao, and Baoquan Chen

Abstract—3D printed objects are rapidly becoming prevalent in science, technology and daily life. An important question is how to obtain strong and durable 3D models using standard printing techniques. This question is often translated to computing smartly designed interior structures that provide strong support and yield resistant 3D models. In this paper we suggest a combination between 3D printing and material injection to achieve strong 3D printed objects. We utilize triply periodic minimal surfaces (TPMS) to define novel interior support structures. TPMS are closed form and can be computed in a simple and straightforward manner. Since TPMS are smooth and connected, we utilize them to define channels that adequately distribute injected materials in the shape interior. To account for weak regions, TPMS channels are locally optimized according to the shape stress field. After the object is printed, we simply inject the TPMS channels with materials that solidify and yield a strong inner structure that supports the shape. Our method allows injecting a wide range of materials in an object interior in a fast and easy manner. Results demonstrate the efficiency of strong printing by combining 3D printing and injection together.

Index Terms—3D printing, minimal surfaces, inner structures, injection

1 INTRODUCTION

Recent years have seen a growing interest in 3D printing technologies, capable of generating tangible solid objects from their digital representation. Common to the process of 3D printing, in addition to the external surface of the object that is printed, its inside is also filled by some material following the pattern of certain inner structures. Choices for the pattern of the infill are made based on the properties to be achieved such as durability and strength [1], material economy [2], [3], or 3D printing performance [4].

Interior scaffolding is the process of replacing the solid interior by skeletal elements and truss scaffoldings that support the exterior boundary [5], [6]. To realize strong and lightweight 3D manufacturing, various infill structures and scaffoldings have been proposed. Techniques, ranging from straightforward local hollowing [7] to special property structures such as honeycombs [1] shown to be effective in achieving lightweight yet strong interior support. Works in this field focus on interior optimization which is a challenging task involving careful design of the interior support especially in presence of complex geometry and topology. E.g., thin double-walls, high curvature and high genus.

Different from these techniques, we avoid the complexity of computing and positioning intricate support structures in the shape interior. Instead, we take a somewhat different approach which assumes a closely hollow 3D object that is injected with strong materials. Thus, object strength and durability is achieved simply by choosing the appropriate injection material. As a result, strong 3D printing reduces

to the task of computing injection channels that properly distribute the injected material in the object interior.

For this purpose, we explore triply periodic minimal surfaces (TPMS) to define injection channels as globally controllable structures. TPMS are smooth, connected and self-supported parametric surfaces that allow good control and thus have been considered as scaffolding structures in various domains [8], [9], [10], [11]. Drawing inspiration from these works, we utilize TPMS to define smooth hollow channels in the object interior that are 3D printed together with the object. After the object and inner structures are 3D printed, we inject the channels with external materials of any desired property and strength that turn into solid through a simple solidification process (see Fig. 1).

Our 3D printing and injection benefits from TPMS structural properties of smoothness, connectivity and quasi self-supporting. W.r.t. 3D printing this means that the internal TPMS channels are self-supporting, requiring no extra support in the printing process while their connectivity and smoothness allow to easily inject and fill the TPMS channels with different materials.

To summarize, our work makes the following novel contributions:

- A novel 3D manufacturing approach which achieves model strength through injection of strong materials into internal channels.
- Utilization of TPMS to allow easy generation of inner channels. TPMS are closed form and therefore easily computed, requiring merely to manipulate an implicit function. TPMS distribution inside the object is controlled by adjusting their frequencies, generating an adaptive structure.
- Efficient and simple 3D printing of strong objects. TPMS yield self supported inner channels that can be printed in a straightforward manner. In post-processing they are injected with strong materials. TPMS smoothness and connectivity guarantees their full injection.

- *Xin Yan, Cong Rao, Lin Lu, and Haisen Zhao are with the School of Computer Science and Technology, Shandong University, Shandong, China.*
- *Andrei Sharf is with the Department of Computer Science, Ben-Gurion University. E-mail: asharf@gmail.com*
- *Baoquan Chen is with Peking University and Shandong University. E-mail: baoquan.chen@gmail.com*
- *Xin Yan and Cong Rao are joint first authors.*
- *Corresponding author: Lin Lu (lulin.linda@gmail.com).*

Manuscript received September 27, 2018.



Fig. 1. The interior TPMS channel of a 3D kitten is injected with strong blue resin. The translucent rendered 3D kitten with optimized interior TPMS channel (leftmost), the 3D printed kitten sliced for visualization purposes of the TPMS channel structure (mid) and infill distribution (rightmost).

2 RELATED WORK

The computation and optimization of interior structures such as scaffolding and porous has been widely investigated in the context of CAD, solid modeling, material design and tissue engineering. A survey [12] studies state-of-the-art methods for fabrication aware design. Readers are also referred to the recent book [13] for further information. In the following, we discuss related methods focusing on lightweight structural optimization, minimal surfaces and multiple material fabrication and injection.

Interior structure optimization. Structure synthesis and scaffolding have been extensively explored in tissue engineering and computer-aided design [14], [15]. Engineers have developed lightweight structural cores (i.e., honeycomb, balsa and foam) to reduce weight and enforce strength [16]. For example, honeycomb cores have shown material-efficiency thanks to their hexagonal cell configuration [17].

Structural optimization of object interiors has been used to improve strength and reduce printing costs [7]. In their work, authors define an iterative optimization process where supporting struts, thickening and hollowing are applied to sustain stress and grip forces.

Reducing the object's interior material is an important property for reducing 3D printing costs and duration. Nevertheless, it should be tightly coupled with strength characteristics of the object to guarantee the physical object durability. In their work, Zhou et al. [18] identify structural problems in objects by building a weakness map to measure the shape response to worst-case external pressure.

Similarly, in [5], the solid interior of an object is completely replaced by an optimized truss scaffolding. To overcome lack of stability, Prévost et al. [19] carve the interior volume to improve its equilibrium. They define the shape's interior modification as an energy minimization problem to optimize balance. Lu et al. [1] introduce a hollowing optimization algorithm based on the concept of honeycomb-cells structure. They compute irregular honeycomb-like volume tessellations which define the inner structure by optimizing the strength and weight of the object. Zhang et al. [20] use a data-driven method to compute a non-

uniformly hollowed shape to realize the desired bending behaviors.

Topology optimization is also a widely used approach, which iteratively removes and redistributes material from a part while obtaining minimum compliance and keeping it lightweight [21], [22], [23], [24], [25], [26]. Wu et al. [27] adapt the topology optimization by restricting the computational domain to a hierarchical grid of rhombuses, such that the result infill structures are self-supporting. However, the essential problem hindering topology optimization method from our fluid injecting idea is that, there is no theoretical guarantee that the interior structures are smooth and free of local maxima along the injecting direction, which would cause the injection easily jammed.

In this context our work also analyzes stress and strength factors for the purpose of interior optimization and strong objects generation. Nevertheless, our method takes a step further by enhancing object interiors with injected natural or synthetic materials. This defines a novel interaction with multiple materials that is guided by the 3D printed frame and leverages 3D manufacturing.

Minimal surfaces and scaffold engineering. Minimal surfaces have been studied extensively in the context of materials science and mechanical engineering [28]. In computer graphics, minimal surfaces have been introduced as novel modeling tools for animating dynamic liquid foams (e.g., coffee foam) [29] and double bubbles [30]. Pérez et al. [31] explored the Kirchhoff-Plateau Surfaces in the context of fabrication, designed planar rod networks embedded in pre-stretched fabric that deploy into complex, three-dimensional shapes.

Triply periodic minimal surface (TPMS) is a subset of minimal surfaces that extend periodically and indefinitely in space [32], [33]. The TPMS structures and related geometries widely exist in natural systems, and have attracted great interest in materials science due to the optimized physical properties [34]. Compared to other porous structures, TPMS structures have the main advantages of easy controllability, high-smoothness and full-continuity.

Significant progress has been made to investigate the mechanical properties and energy absorption abilities of the TPMS structures after fabrication [35], [36], [37]. Ra-

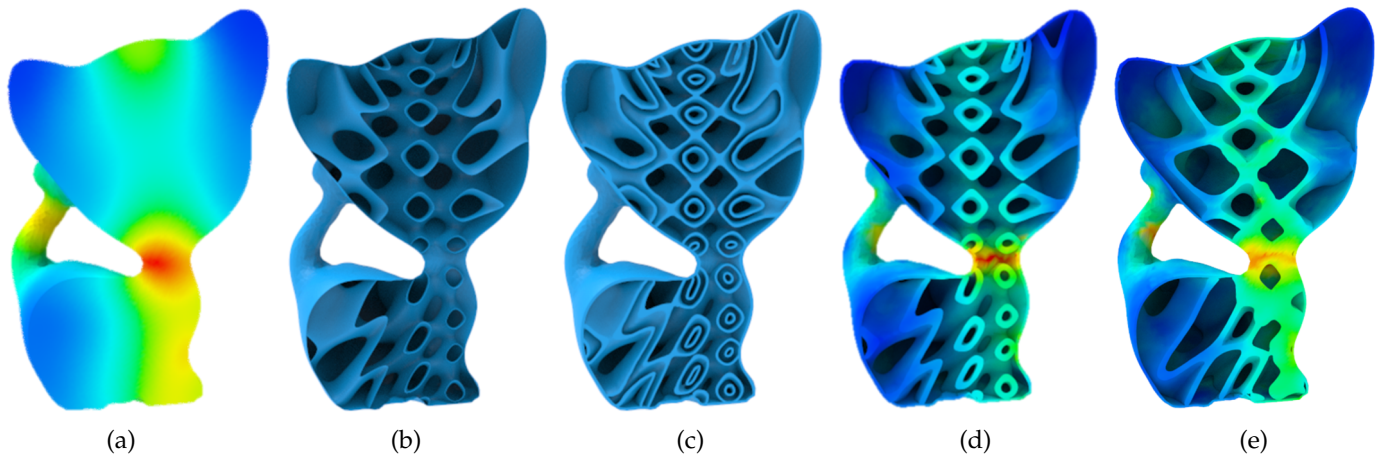


Fig. 2. Given a 3D shape and its external forces, we compute its stress field (a) and generate an adaptive TPMS in its interior (b). We compute a TPMS channel by offsetting the TPMS yielding a dual sheet like structure (c). We recompute the stress field considering the interior structure (d) and optimize TPMS frequency and channel width such that the resulting channel sustains the given forces when injected (e).

jagopalan and Robb [8] utilize TPMS to construct 3D scaffoldings, exploring mechanical properties of their porous structure. Melchels et al. [9] investigate TPMS-based scaffolds by utilizing different materials and pore architectures in the 3D printing process. Their results in the context of tissue engineering scaffolds show a large freedom of design, and properties ranging from rigid and strong to highly flexible and elastic structures. To control the internal TPMS porosity and structure, Yoo et al. [10] propose a modeling algorithm that uses a distance field and boolean operations. Thus, pore size, porosity, and structure type can be locally controlled while preserving connectivity across the entire scaffold. A recent work [38] takes gyroid as the basic cell and applies topology optimization strategy to find the optimum density distribution of the cellular structures.

In this work we control the TPMS distribution and thickness in the object interior according to stress features. Furthermore, smoothness and connectivity features of TPMS are exploited as the injected material expands and smoothly fills the interior.

Our work is also related to the design and synthesis of microstructures. Standard periodic microstructures [39], [40] are tiled in the object’s interior, to produce a particular homogenized elastic behavior. Procedural, aperiodic microstructures like Voronoi foams [41], [42], [43] are also investigated to achieve prescribed isotropic, or orthotropic elasticity. Panetta et al. [44] propose a parametric microstructure model, such that the stress concentrations in microstructures can be minimized, via evolving the shapes in both thickness or topologies.

Multiple material fabrication and injection. While the majority of 3D printers use only a single material at a time, we observe a substantial progress in the class of multi-material 3D printers (e.g., Connex Objet, Stratasys PolyJet™) which are currently capable of generating composite materials with complex structures.

Vidimce et al. [45], [46] propose a shader-like language for multi-material content creation. The pipeline supports procedural evaluation of geometric detail and material composition, allowing models to be specified efficiently. Skouras et al. [47] target for designing actuated characters with

desired deformation behavior, and combine silicone injection molding with 3D printing together during the fabrication. Air injection was considered recently in the context of design and fabrication of soft pneumatic objects [48]. Given a 3D object with its rest and deformed target shapes, the object volume is optimally modelled with a set of chambers that are controlled with air injection by a pneumatic system.

Recently, a method for designing and fabricating metasilicones was introduced [49]. In order to control silicone strength and stiffness properties, the authors inject spherical inclusions of a liquid material into the silicone. By varying the number, size, and locations of these inclusions as well as their material, different properties of silicone objects can be achieved.

Similar to us, hot melt adhesive (HMA) materials were injected into 3D printed materials and their strength was tested [50]. Nevertheless, in their work, authors do not attempt to control interior material distribution which is a key feature in our work using TPMS channels.

Although the spectrum of materials that can be 3D-printed is steadily increasing, there are still many limitations, especially when it comes to advanced materials. Whether filament-, resin-, or powder-based-3D-printed materials are still far away from the level of quality offered by natural or synthetic polymers. This also explains the increasing attention on techniques for silicone molding [51], [52], [53], which help relax restrictions on the shape that can be fabricated by traditional molding. However, it cannot replace additive manufacturing.

3 OVERVIEW

Given a 3D shape and its external forces, we compute an optimized TPMS channel in the shape interior such that the injected fluid smoothly propagates and fills it. As the material solidifies, the 3D printed object is generated as a combination of two solid materials. Our method optimizes the TPMS channel structure to guide the interior material distribution and sustain strength requirements and resist predefined stress factors (see Fig. 2).

Initially, we perform structural analysis on the shape volume using the finite element method (FEM) and compute

a stress field. We use the stress field to guide our TPMS-channel optimization. I.e., we compute a non-uniform TPMS periodic function in the shape interior which defines the channel structure, controls material distribution and consequently governs object strength.

TPMS-channel optimization is controlled by two parameters: periodicity P governing channel oscillations and width W governing local material capacity. The rationale here is that channel oscillations (i.e. frequencies) control channel density in the interior. High frequencies yield a dense distribution of TPMS channels in the interior allowing to protrude narrow regions. Nevertheless, high frequency channels are limited in their width due to self-intersections while low frequencies allow wider channels which in turn distribute more filling material into weak regions (see the kitten's neck in Fig. 2(e)).

Once the initial TPMS structure is computed the stress field needs to be updated as the shape mass distribution changes possibly yielding a different stress map. This may require an iterative refining process of the TPMS frequencies according to new stress fields. To solve it, we cast the problem into a non-linear optimization.

Starting from the initial TPMS channel with a uniform width, we optimize the structure iteratively. In each iteration, we optimize channel widths and TPMS frequencies in an interleaving manner. The stress field is updated in each iteration based on the FEM of the two materials. Iterations stop when the model can sustain the required stress factors with optimized volume or get fully injected with the fluid.

In the final step, we create an entry point on the surface for injecting the filling material inside the channel (and corresponding exit point for air escaping). Using a visibility map, we search for the least visible region of the object for creating the entry point in order to least interfere with shape visual appearance, (Algorithm 1).

Algorithm 1 TPMS Channel Optimization

Input: A 3D shape S , external forces F .

Output: Fabricatable TPMS channels TC in S .

- 1: Compute the stress field $SF(S, F)$ via FEM;
 - 2: Compute the periodicity $P(\mathbf{x})$ from $SF(S, F)$;
 - 3: Channel width $W \leftarrow W_0$, generate $TC(P(\mathbf{x}), W)$ in S ; (Sec.4.1.1)
 - 4: Optimize the connectivity and self-supportness of TC ; (Sec.4.1.3 & 4.1.4)
 - 5: **while** $SF(S, TC, F) > \chi$ && $\mathcal{V}(TC(P(\mathbf{x}), W)) < \mathcal{V}(S)$ **do**
 - 6: Optimize TC to be self-supporting;
 - 7: Optimize TC on W ; (Sec.4.2.1)
 - 8: Optimize TC on $P(\mathbf{x})$; (Sec.4.2.2)
 - 9: **end while**
 - 10: Generate entry and exit points; (Sec.4.3)
 - 11: **return** TC .
-

4 TECHNICAL DETAILS

Our method consists of computing channels in the shape interior to correctly guide the propagation of injected material and create the desired support structure. Channels are defined by solving a closed form implicit surface in the shape interior w.r.t. a constrained minimization.

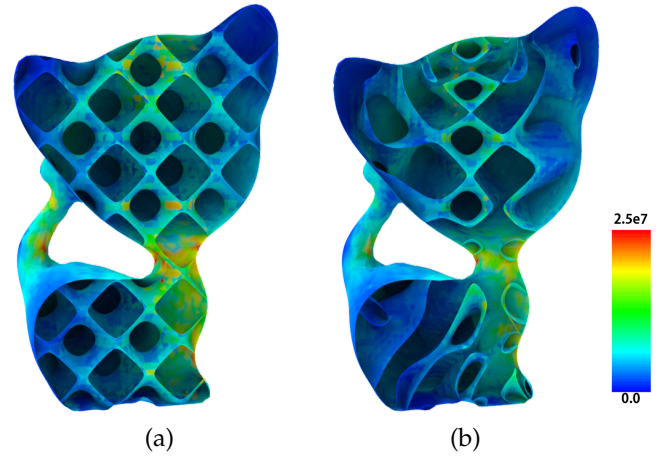


Fig. 3. A kitten model with uniform periodicity TPMS (a) vs. adaptive periodicity TPMS (b). The two models are of the same volume.

4.1 Adaptive TPMS-Channels

A triply periodic minimal surface (TPMS) is a periodic implicit surface defined independently in three orthogonal directions. It defines a large family of surfaces which all have a closed form implicit representation that results from convolving sin and cos terms along x , y , and z axes. We choose to use here the Schwarz P-Surface due to its simplicity and having a minimal genus among all triply periodic minimal surfaces.

P-Surfaces have been a common choice for prototyping tissue scaffolds due to their large fluid permeability [54], [55] and high surface-to-volume ratio and strength [11]. The general form of P-surface is defined by the zero-value level-set of the function:

$$F(\mathbf{x}) = \cos\left(\frac{2\pi}{P(\mathbf{x})} \cdot x\right) + \cos\left(\frac{2\pi}{P(\mathbf{x})} \cdot y\right) + \cos\left(\frac{2\pi}{P(\mathbf{x})} \cdot z\right) = 0, \quad (1)$$

where $\mathbf{x} \in S$ is the position with coordinates (x, y, z) , and $P(\mathbf{x})$ controls the periodicity of the TPMS. We denote $P(\mathbf{x})$ as the periodicity function (i.e. 1/frequency) of the TPMS.

4.1.1 TPMS-channel control parameters

The rationale behind our channel control is that injected material should be distributed in weak regions more than in strong regions. Note that since the TPMS structure is locally uniform, its support is omni-directional. Thus, given a 3D shape $S \subset R^3$, its interior TPMS channel is denoted as $TC(P(\mathbf{x}), W)$, where $P(\mathbf{x})$ and W are parameters governing TPMS periodicity and channel width (i.e. diameter) respectively. Both parameters control the injected material distribution, $P(\mathbf{x})$ controlling the overall channel density and W fine tuning the channel capacity in a rather local scale. We also denote the TPMS patch with no thickness by TP for exposition, i.e., the structure of $TC(P(\mathbf{x}), W)$ is governed by $TP(P(\mathbf{x}))$.

To generate the initial TPMS-channel distribution, we map $P(\mathbf{x})$ to a continuous function derived from the shape stress field. Intuitively, $P(\mathbf{x})$ has negative correlation with the stress value, i.e., TPMS-channel distribution is dense in weak regions with high stress values.

Stress field is initially computed on the fully solid object based on FEM. It is defined by the von-Mises stress values,

denoted by $\rho(\mathbf{x}) \in (0, 1]$ which is smoothed and normalized. Thus, $P(\mathbf{x})$ is initially defined as:

$$P(\mathbf{x}) = \frac{\alpha}{\rho(\mathbf{x})^{1/3}}, \quad (2)$$

where α indicates the minimal period size in the TPMS structure (in all our experiments $\alpha = 8mm$).

In our experiments, we set the initial TPMS channel with the minimal capacity, i.e., we assign $W = \{2mm\}$ uniformly to all sample points on the TPMS patch TP , which is the minimal value that the fluid can smoothly flow, based on our experiments.

Fig. 3 shows a comparison between uniform and adaptive TPMS channels. While both models have the same total volume, the adaptive TPMS channel guided by the stress field has a significantly better interior material distribution in terms of strength values (e.g. see Kitten's neck).

4.1.2 TPMS smoothing mask

The TPMS is globally determined by the periodicity function $P(\mathbf{x})$ in Eqn. 2, and bounded by the shape interior S . To optimize the TPMS structure w.r.t. stress field, we locally adjust the surface frequency. Nevertheless, such local refinement should conform to TPMS properties without violating global smoothness.

To allow such local refinement, we utilize a smoothing mask $M(\mathbf{x})$ defined by a set of control points $\{p_i\}_{i=1}^m$ sampled on TP by the volume grid. For each control point p_i , we define a smoothing gaussian kernel:

$$M_i(\mathbf{x}) = e^{-\frac{\|\mathbf{x}-p_i\|^2}{2\sigma^2}}, \quad (3)$$

where the variance parameter σ is set to $0.25P(p_i)$ in all our experiments.

$M_i(\mathbf{x})$ can be regarded as an influence mask governed by the control points p_i which essentially smooth the TPMS periodicity. We sum up all kernel functions driven by the control points $M(\mathbf{x}) = \sum_{i=1}^m M_i(\mathbf{x})$, normalize it, and use it as a local tuning operator.

4.1.3 TPMS-channel connectivity

In the process of bounding the TPMS-channel to the shape interior, we intersect it with the shape boundary possibly resulting in disconnected channel components. A multitude of disconnected channels would require separate optimization and handling resulting in costly processing and injection time.

To reduce the number of channel components to a minimum we tune the TPMS frequency such that the channel oscillations stay maximally connected in the interior (see Fig. 4). Specifically, we gradually increase TPMS frequencies of the smallest area component until its surface connects to another component thus becoming of larger area. We repeat this process for the next smallest area TPMS component.

For the identified TPMS component, we locate the sample points it covers and compute $M(\mathbf{x})$. Then, we gradually tune the periodicity function $P(\mathbf{x})$,

$$P(\mathbf{x}) := P(\mathbf{x})(1 - kM(\mathbf{x})), \quad (4)$$

where the step size $k = 0.05$ in our experiments. The stop condition for local tuning of a TPMS component is that it connects with other components and its surface increases.

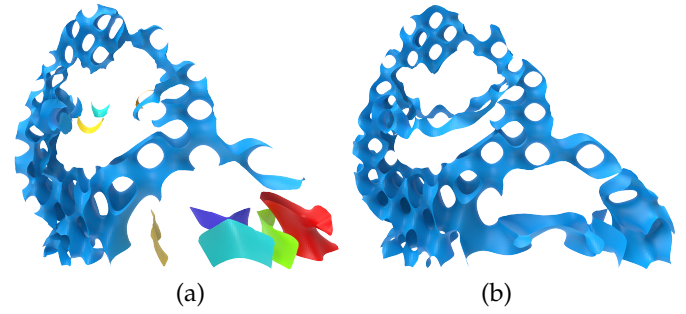


Fig. 4. The fertility model has multiple TPMS channels due to intersections of TPMS with the surface (a). We locally increase frequencies at disconnected channels to obtain one connected channel (b).

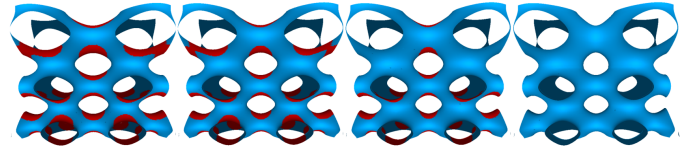


Fig. 5. Local self-support optimization of the TPMS structure from left to right. The physical size is 14^3cm^3 and step size is $k = 0.2$. Areas that need support are highlighted in red.

Note that the connectivity enforcement does not always guarantee a single fully connected TPMS-channel. For example, in cases where the shape has thin and small interiors, the TPMS channel may disconnect while intersecting with the shape surface. Nevertheless, this does not pose a problem as our method can handle multiple disconnected TPMS-channels independently.

4.1.4 Self-supportness

Theoretically, TPMS structures are quasi self-supporting everywhere when defined with constant periodicity on isotropic domains. In our case, TPMS are defined in the interior of arbitrary shapes and may stretch and deform due to varying local frequencies and amplitudes. This may yield unsupported TPMS parts during their fabrication.

Unsupported regions in additive manufacturing are defined by the overhang concept which requires evaluating the angle between the local normal and the additive manufacturing direction, called *subtended angle* [56].

We set the subtended angle threshold in our experiments to 145° for FDM (i.e., unsupported structures occur if the subtended angle exceeds 145°). We define a tolerance for overhang regions, since small overhangs do not need support. We set the tolerance area as $16mm \times 16mm$ for FDM, i.e., if the overhang region area is smaller than this area it is considered as self-supporting.

We avoid unsupported overhanging parts in the TPMS computation by decreasing the amplitude of the TPMS structure along with the additive manufacturing direction. We assume that the positive z -axis is the build direction and introduce a tuning function $\gamma(\mathbf{x})$ that locally controls and decreases the TPMS amplitude in the z -axis:

$$\mathcal{F}(\mathbf{x}) = \cos\left(\frac{2\pi}{P(\mathbf{x})} \cdot x\right) + \cos\left(\frac{2\pi}{P(\mathbf{x})} \cdot y\right) + \gamma(\mathbf{x}) \cos\left(\frac{2\pi}{P(\mathbf{x})} \cdot z\right) = 0, \quad (5)$$

$$\gamma(\mathbf{x}) := \gamma(\mathbf{x})(1 - kM(\mathbf{x})). \quad (6)$$

The mask function $M(\mathbf{x})$ here is determined by the sample points on TP that need support.

This way, we avoid overhanging regions that exceed the subtended angle threshold and the TPMS structure is guaranteed to be self-supporting (see Fig. 5).

4.2 TPMS-channel Optimization

Injected material flow capacity and distribution is controlled by the channel parameters. Thus, given a TPMS-channel $TC(P(\mathbf{x}), W)$, $P(\mathbf{x})$ governs channel periodicity (i.e. oscillations) and W governs channel width (i.e. W defines a set of local widths w_i that are assigned for each sample point p_i on the TPMS patch $TP(P(\mathbf{x}))$).

Our optimization consists of searching in a highly non-linear functional space of stress and volume that are controlled by P and W . In Fig. 6 we plot the functional space of the TPMS-channels in the kitten model. Top shows four samples of the interior channel and the resulting stress.

The transparent plane in Fig. 6 indicates the yielding value. Only models below this plane are regarded as stable, among which sample c has the minimal volume i.e., the minimal material cost.

To visualize the functional space, we uniformly sample both P and W yielding different TPMS-channel configurations. Specifically, periodicity P is sampled in the range of 5mm to 65mm with 5mm interval. Width W is sampled in the range of 2mm to maximal value without self-intersections with 2mm interval. The surface in Fig. 6 is interpolated by 84 samples totally. The stress in the vertical axis is computed as the average of the 1% maximal stress values for each model.

Intuitively, high frequency TPMS yield dense channel structures that enable them to protrude into narrow regions of the shape interior (in Fig. 6 d). In contrast, low frequency TPMS define coarser structures with small oscillations which allows to create wider channels as self-intersections are less prevalent (in Fig. 6 a).

Width and volume have positive correlation. Nevertheless, the relation between stress and width is non-monotonic and non-linear (in Fig. 6 a & b have the same P). Similarly periodicity and volume have negative correlation as decreasing the periodicity results in volume increase (in Fig. 6 a & d have the same W). In the majority of cases dense TPMS-channel distribution reduces the stress, however the general relation between stress and periodicity is non-monotonic and non-linear.

Our optimization initializes with a high frequency TPMS enabling channels to protrude narrow regions yielding fine-scale channels everywhere (see Section 4.1.1). Next, periodicity and widths are locally optimized to account for the correct stress support. We perform structural analysis using FEM-based von Mises stress with two materials: the 3D printing material and the injected one. Then we iteratively solve the optimization problem with the following objective function:

$$\operatorname{argmin} \mathcal{V}(TC(P(\mathbf{x}), W) \text{ s.t. } SF(S, TC, F) < \chi \quad (7)$$

where $\mathcal{V}(\cdot)$ is the total volume of the TPMS channel, $SF(S, TC, F)$ is the stress field computed from S with TPMS channels and injected materials under the external

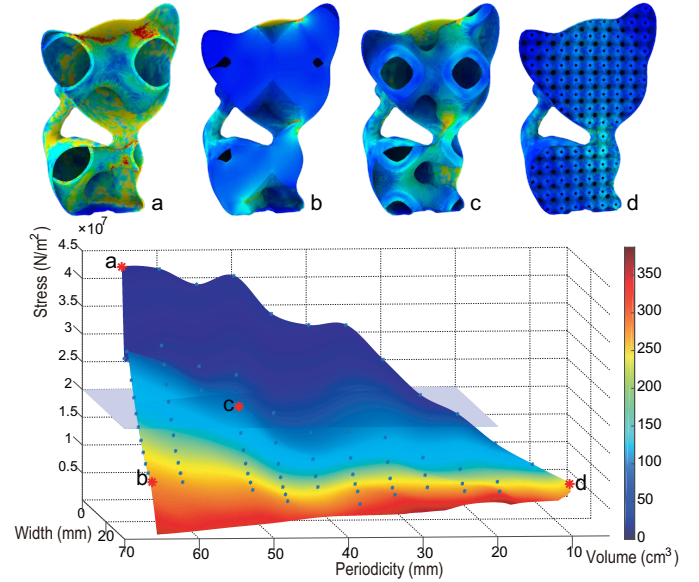


Fig. 6. The functional space of the kitten model, showing stress and volume as functions of P and W . Top are four samples from the functional space colored by the stress value. Our optimization searches for the lightest volume (color) with overall stress below a given yielding point (intersecting transparent plane).

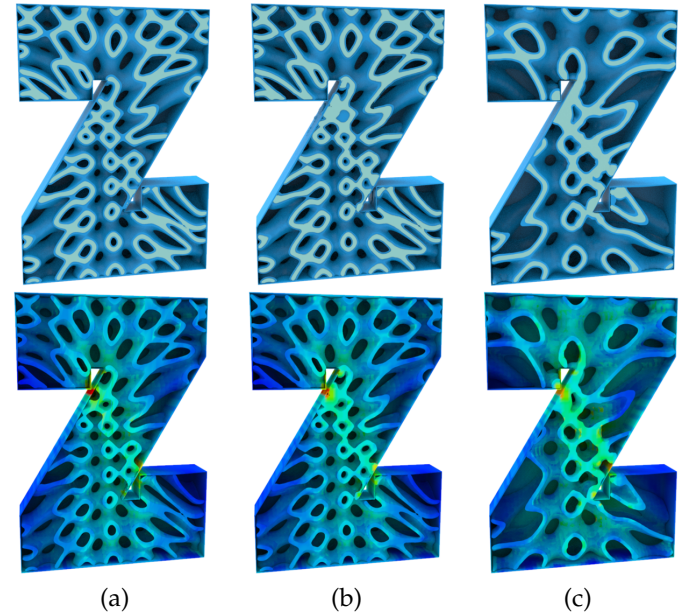


Fig. 7. Illustrations of TPMS channel optimization. Starting with dense TPMS frequencies and a uniform channel width (a), we tune the width to increase the strength on a fine scale (b) and decrease the frequency on a coarse scale (c). The injected materials are highlighted in the upper row.

forces F , and χ is the yielding value for the material. Here we use the yielding value for the printing material, as a safe threshold. In each iteration, the stress field needs to be updated since the optimization changes the internal structure and mass distribution.

We independently solve the optimization problem for $P(\mathbf{x})$ and W on two scales. On a coarse scale we optimize $P(\mathbf{x})$ and on a fine-grained scale, we optimize W keeping $P(\mathbf{x})$ constant. Intuitively, TPMS frequencies govern the

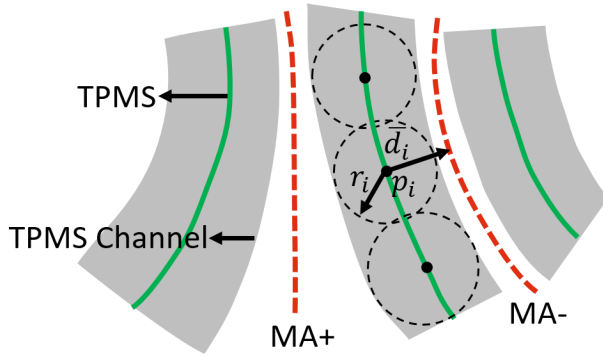


Fig. 8. Illustration of the width control of the TPMS channel. The width w_i of sample point p_i can be regarded as the diameter of the local sphere on p_i , i.e., $w_i = 2r_i$. The upper bound of w_i is $2\bar{d}_i$. MA+ and MA- indicate the medial axis of the positive component and negative component defined by the TPMS function.

global interior structure while channel widths allow a more local fine-grained optimization (see Fig. 7). The stopping criteria is that no weak regions are left in the model or the capacity of the TPMS channel cannot be further enlarged.

4.2.1 Width optimization

The width variable allows to locally tune the TPMS-channel diameter. The local width is upper bounded to avoid self-intersections. Thus, for each sample point p_i on TP , we compute its width upper bound \bar{w}_i derived from the minimal value among distances from p_i to the medial axis (MA) of the two sides of the TPMS surface (see Fig. 8):

$$\bar{w}_i = 2\bar{d}_i = 2 \min(\text{dis}(p_i, \text{MA}+), \text{dis}(p_i, \text{MA}-)). \quad (8)$$

The TPMS patch TP defined by $\mathcal{F}(\mathbf{x}) = 0$ (Eqn. 5) divides the space into two parts, the positive one ($\mathcal{F}(\mathbf{x}) > 0$) and negative one ($\mathcal{F}(\mathbf{x}) < 0$). To fast compute the distance from the sample point p_i to MA+ in the positive space and MA- in the negative space, we construct the signed distance field, denoted by $f(d) = \{x | \text{sgnd}(x, TP) = d\}, d \in R$. Then the distance in Eqn. 8 is approximated as follows, without explicitly computing MA+ and MA-.

$$\begin{aligned} \text{dis}(p_i, \text{MA}+) &= \max_d (\text{sgnd}(p_i, f(d) = d), d > 0), \\ \text{dis}(p_i, \text{MA}-) &= -\min_d (\text{sgnd}(p_i, f(d) = d), d < 0). \end{aligned} \quad (9)$$

In each iteration we test all sample points p_i w.r.t. their stress values in their proximity (we use the sphere defined by radius r_i here). If p_i is in the proximity of a weak region defined by the yielding value χ , we increase its width w_i by δ as long as w_i is below its upper bound \bar{w}_i . We use $\delta = 2\text{mm}$ in the experiments.

The stopping condition of width optimization iterations is that no weak regions are left, or no w_i can be further increased (due to self-intersections).

4.2.2 Periodicity optimization

The principle behind optimization of TPMS frequencies is to decrease frequencies thus allowing larger channel widths and more injected material in weak regions (while reducing materials in strong regions). Therefore, we minimize Eqn. 7 with the variable $P(\mathbf{x})$ in a heuristic manner. For strong

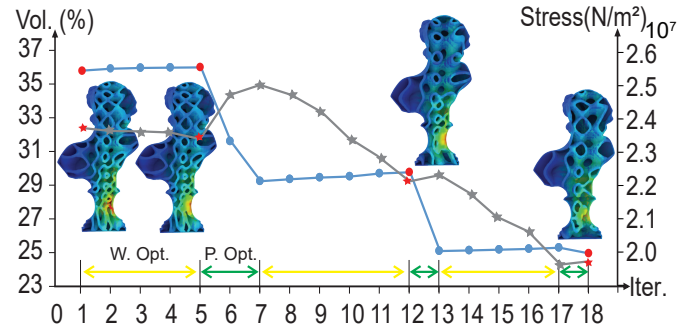


Fig. 9. Optimization of volume material (blue curve) and maximal stress (gray curve) along with iterations for the Sappho's bust model. TPMS-channel structures are shown for iterations indicated by red dots on the curves.

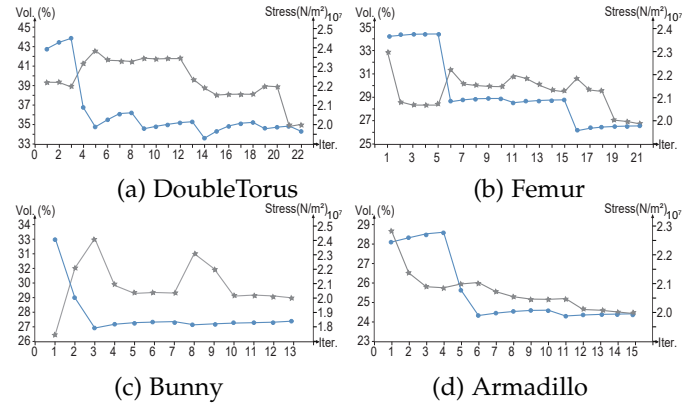


Fig. 10. Plots of the volume material (blue curve) and maximal stress (gray curve) along with optimization iterations for the models in Fig. 17.

regions, increasing periodicity to reduce channel capacity and material is regarded as the gradient descent direction. For weak regions, increasing periodicity allows wider channels such that more materials can be injected. Thus, stress may not monotonically reduce along optimization process as slight increase in the stress value may occur during periodicity optimization of the weak regions.

For each sample point p_i on TP , we use the local sphere with radius r_i to define its neighborhood range as above. If the stress value is larger than χ , i.e., in weak regions, or smaller than a given threshold (1.5MPa in our experiments), i.e., in strong regions, we mark it as the local control point. For all such local points, we form the mask function $M(\mathbf{x})$. Then the periodicity for the TPMS structure is iteratively increased following:

$$P(\mathbf{x}) := P(\mathbf{x})(1 + kM(\mathbf{x})), \quad (10)$$

where $k \in R^+$ is an adaptive step size starting from 0.05 and gradually diminishing to zero. The stopping condition is that further increasing would drive the TPMS in S disconnected. The self-supporting checking and treatment is performed after each iteration.

4.2.3 Optimization convergence

The width and periodicity optimizations are performed in an interleaving manner. During width optimization total volume increases while stress is relieved in weak regions. During periodicity optimization, material volume decreases

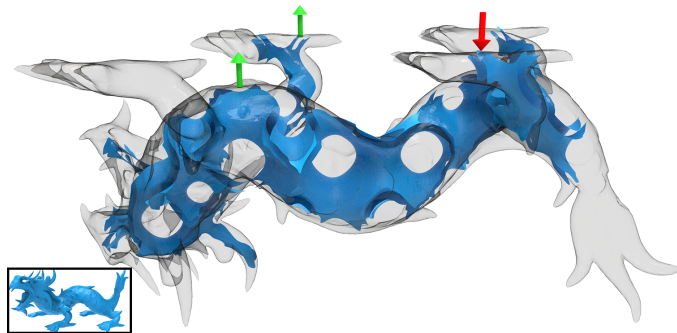


Fig. 11. Entry and exit points computation on the dragon model (bottom left). The red arrow indicates the entry hole and the green arrows are the air vents.

in strong regions, balancing between strength and weight. In the last stage the stress is below the yielding value and periodicity is optimized to further reduce volume. Fig. 9 illustrates the optimization behavior of the TPMS-channel parameters ($P(x)$ and W) along iterations on width ($W.Opt.$) and periodicity ($P.Opt.$). See Fig. 10 for more models. Note that in Fig. 9 and 10, we only plot the volume and stress on the TPMS channels without the shape boundary shell.

In most cases, our non-linear optimization converges quickly due to two independent optimizations performing on different scales. Starting from the initial TPMS channel, each model typically needed 2-3 rounds for adjusting the TPMS frequencies at a coarse level and 3-4 rounds for fine tuning the channel capacity. In each round for either width or periodicity optimization, the number of iterations varies depending on the stress distributions. The total number of required iterations depends on the external forces, boundary conditions, and the step size for both loops.

We note that theoretical convergence is not guaranteed in our algorithm. For instance, oscillations may be introduced if the step size is too large between $W.Opt.$ and $P.Opt.$ Also, the self-support checking and treatment after each round may cause oscillations, especially when the forces directions are of large variance with the printing direction.

4.3 TPMS-channel Generation

The TPMS-channel is realized by a double sheet structure obtained through offsetting the TPMS surface in positive and negative normal direction. Channel width defines the offset distance between the two sheets and indicates the capacity of the injected fluid material.

As shown in Fig. 8, w_i is regarded as the diameter of the sphere locates on p_i , such that the TPMS channel is actually the exterior envelop of the series of spheres.

Once the TPMS periodicity function $P(x)$ and width W are determined, the TPMS-channel $TC(P(x), W)$ can be reconstructed using marching cubes (see Fig. 2b-c). In practice, we discretize the shape volume into a 200^3 grid resolution, and use standard marching cubes to compute the zero level surface corresponding to the offsetted TPMS sheets.

Entry point computation. For each connected TPMS channel inside the shape, we create an entry point on the surface for injecting the filling material. Using a visibility map, we

search for the least visible region of the object for creating the entry point in order to least interfere with shape visual appearance. Once the entry point is positioned, we compute the model orientation for injection and follow the method in [51] for locating the exit points, to ensure that the air exits properly during the material injection. The basic idea is to assign each vertex with a shaking cone along the gravity direction and search for the smallest set of maxima that cover all vertices. We use the shaking angle as 40° .

Since points on the minimal surface are all saddles with opposite principal curvatures, the maxima only exist on the intersections between the TPMS channel and the shape boundary. Thus, we only need to put air vents on the shape boundary, i.e., the interior of the channel is smooth with no bottlenecks. Similarly, using the TPMS smoothness characteristics, we also guarantee a proper fluid flow in the channel (see Fig. 11). The diameter is 5mm for the entry holes and 1mm for the air vents in our experiments.

5 RESULTS

We evaluate our method by computing interior TPMS channels for a large variety of 3D models. In our experiments, we 3D print the objects, fill their interior by injecting several fluid materials. After their solidification, we test the strength of these objects by applying forces and measuring their durability.

We run our method on an Intel Core™ i7-6700K CPU @ 4.0GHz and 16 GB RAM. In our experiments, computation time for the TPMS channel optimization were in the range of 1-4 hours depending on the shape geometry complexity and the external forces. The most time consuming step in our method is the FEM structural analysis, which highly depends on the number of elements. For efficiency reasons, we downsample the discretized 3D volumetric space using a 70^3 grid resolution. We use OOFEM library [57] for computing the stress field with two materials, taking each voxel as the computational element. Each element is assigned to either printing or injected material, with different Young's moduli. Both materials are considered with linear elastic behavior. The FEM computation cost largely varies, e.g, it takes 4 minutes for 12k voxels for the Sappho's bust model, and 22 minutes for 42k voxels for the bunny model. Nevertheless, in most cases the number of voxels decreases along with the optimization.

In our experiments, all the models are with the height 15cm. The thickness of the TPMS shell is 0.8mm, which is safe for injection without fluid leaking. We fabricated the result models using an FDM-based printer in PLA plastic materials, whose yielding value is $\chi = 2e7N/m^2$.

Materials Selection. There are many choices for injected fluid materials, as they share the same requirements as molding materials. Nevertheless, we consulted experts in polymeric materials and experimented on a subset of materials representing the wider range. These include liquid silicone rubber (LSR), polyurethane, epoxy resin etc. All materials can be injected in the TPMS channels and solidify at room temperature, while possessing different mechanical properties, solidification time, etc.

The epoxy resin has good properties and is adequate for our injection method. It offers high strength, low viscosity,

and excellent adhesion properties. Therefore, we choose it for the majority of our demonstrations. Actually, epoxy resin has been used as a paint, adhesive or sealant, and also widely seen in industries, like in the manufacture of electronics, electrical components and insulators. Its price is \$2-10 per kilogram, which is significantly lower than PLA (\$25/kg on average) or any other 3D printing materials.

There is yet another common way to further improve the strength of the polymer by adding carbon fibers in it, to form a new composite, called carbon fiber reinforced polymer (CFRP) [58]. We experimented on adding carbon fibers with different proportions in epoxy resin and tested on the strength. The details are listed in Table 1. It shows that epoxy resin and CFRP are much stronger than the PLA material, esp. when mixed with 10% (in mass) carbon fiber, the CFRP offers the best strength.

Based on our experiments, the injected materials are compatible to resin used in SLA-printers, as well as PLA. Fig. 16 shows the kitten model printed in SLA resin and injected by CFRP. Due to the self-supporting property of TPMS, our method is compatible to a large variety of fabrication techniques such as FDM, SLA, and SLS.

Comparisons. We compare the strength of our interior structures filled with strong external materials against the single material object generated by the 3D printer. Naturally, hollow objects consisting of different scaffoldings are weaker than their full counterpart. We use an electromechanical universal testing machine (SANS YAW4605) to physically evaluate the strength of the printed models (see Fig. 12). The crosshead of the machine is controlled to move at a constant speed 5mm/min.

We compared our epoxy resin injected and PLA printed model to a non-injected single material TPMS model and two other models consisting state-of-the-art interior support structures. The four models are of the same volume, i.e., 35% of the full object and 15cm height. As seen from the load-displacement curves (Fig. 13), our injected model is significantly stronger than the non-injected version, i.e., the injected model can afford 12.3KN, while the non-injected model with TPMS channels and PLA printed can afford 4.8KN. The topology optimization model [23] can afford 5KN and the honeycomb-cell model [1] is the weakest and can afford 4.1KN.

We have also tested different external forces and different material settings by running simulations on the different structures. Results are shown in Fig. 14. The Young's modulus for PLA and epoxy resin is set as 1.2GPa and 2.4GPa, respectively and the Poisson's ratio is 0.35 for both materials in the simulation. We use different stress color bar for the injected model (Fig. 14 d) as it has larger yielding value, i.e., 100MPa here. From both physical tests and simulations, we observe that our injected TPMS-channel outperforms other state-of-the-art techniques. Nevertheless, the non-injected TPMS structure performs less good than topology optimization. We also note that since we use a very conservative yielding value (20MPa), the models can afford larger loads in the physical tests comparing with their simulations.

It is non-trivial to adapt general interior structures to the tunnels guiding injected fluid. It must satisfy hard constraints including connectivity, smoothness, free of local maxima on the structure along the injecting direction, and

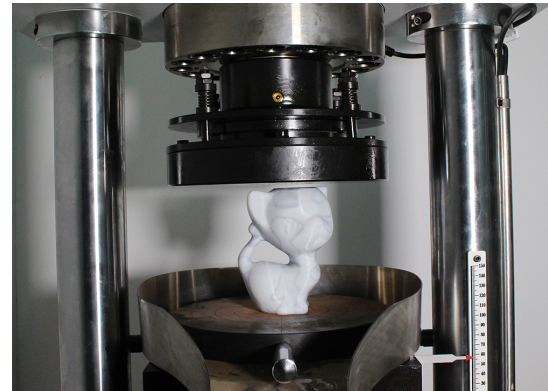


Fig. 12. Our experimental setup for the compression tests. The injected kitten model can afford 12.3KN forces.

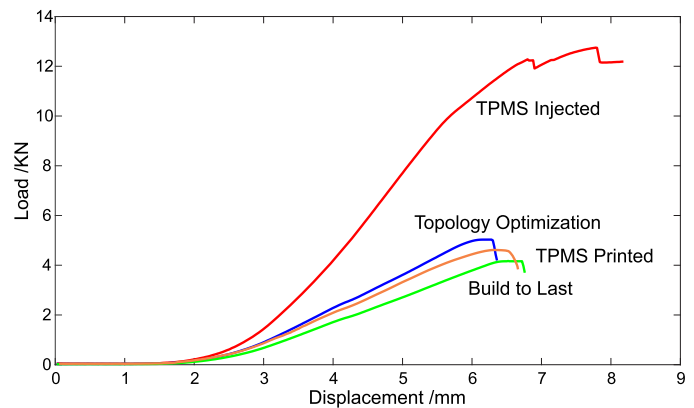


Fig. 13. Load-displacement curves: TPMS channel injected with epoxy resin (red), TPMS channel printed in PLA (orange), topology optimization [23] (blue) and honeycomb-cell [1] (green).

large surface-to-volume ratio for efficient heat dissipation. Although results from topology optimization are mostly connected, they have no guarantee on free of dead ends, which may cause materials jam or air block during injection.

It is an option to fully hollow the model and completely fill the interior with resins. But it limits the selections on injected materials, especially for the resins that produce heat in curing. We tested on filling the fully hollowed model with CFRP. During the curing, the heat flux causes distortions on the shell. While, the TPMS channel has high thermal conductivity due to the large contact area and is free of such artifacts. Moreover, fully injected model may not have the optimal strength because of the self-weight.

Table 2 summarizes the data of all our tests and models, showing a clear advantage of using our strong injected objects. We describe their full volume (SolidV), printed volume (PrintV) and injected material volume (FluidV) in our results, and then the saved materials in the volume ratio (SavedV). Next we measure the printing time of printing the channels and filling them in column (AllPrintT) using an FDM-based 3D printer (layer thickness is 0.2mm). Column (PrintInjectT) measures the time cost for printing the hollow channel with the same 3D printer and afterwards inject with external material. We can see from the last column (SavedT) the significant improvement in material cost and printing time of our technique.

TABLE 1
Experiments on the injected materials. We tested the strength for different compositions of the carbon fiber reinforced polymer (CFRP) and compare with the 3D printed material PLA.

	PLA Shell	PLA Full	Epoxy	CFRP(2%)	CFRP(4%)	CFRP(6%)	CFRP(8%)	CFRP(10%)	CFRP(12%)	CFRP(14%)
Yield Strength	10MPa	49MPa	70MPa	71MPa	97MPa	105MPa	110MPa	112MPa	103MPa	93MPa
Sample										

TABLE 2
Summary of results.

Model	Forces(N)	SolidV.(cm ³)	PrintV.(cm ³)	FluidV.(cm ³)	SavedV.(%)	AllPrintT.(h)	PrintInjectT.(h)	SavedT.(%)
Kitten	3540	422.32	79.97	76.17	63.0	44.1	15.0	66.0
Bunny	3600	667.42	141.30	117.80	53.1	69.3	27.3	60.6
Femur	4800	390.08	77.46	55.68	65.9	40.8	14.2	65.2
Z	6000	596.72	111.12	104.85	63.8	61.1	21.8	64.3
DoubleTorus	4000	166.79	48.39	50.84	40.5	18.1	9.5	47.5
Armadillo	1300	231.62	62.87	35.06	57.7	25.5	13.4	47.5
SapphoBust	900	158.46	39.60	22.83	60.6	17.2	9.2	46.5

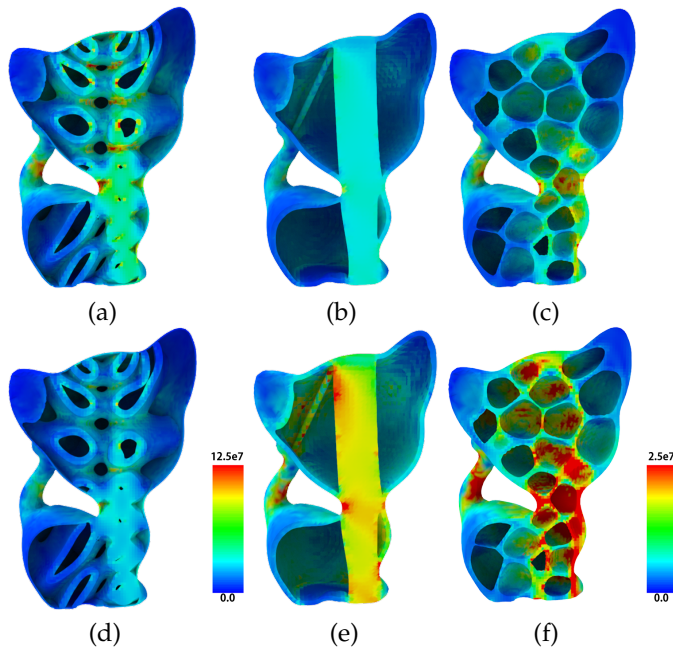


Fig. 14. Simulation results with different material settings and external forces. From left to right: our TPMS channels, topology optimization structures [23], honeycomb-cell structures [1]. (a-c): single material (PLA), with 3KN external force. (d-f): 8KN external force. (d) composes two materials (PLA for the TPMS channel and injected epoxy resin). Except (d), others have the same stress color bar as in the bottom right.

Injection time correlates with channel capacity and for all models, injection time was less than 1 minute (note that all models height is approx. 15cm). Solidification time varies for different injected materials. Polyurethane solidifies very fast in 1-3 minutes while epoxy resin takes longer, i.e., 30 minutes in room temperature for solidification. Compared with printing time, injection time is negligible and can be ignored. In Fig. 15 we show a gallery of 3D printed objects with their interior TPMS channels. Note that printing

two halves is just for demonstration purposes of the inner structures. In practice, the model is printed as a whole (see kitten and bunny results). See also supplementary video for the whole process.

Fig. 17 demonstrates our TPMS channel optimization on various 3D models. From the 3D shape and stress map (leftmost col), we generate the initial non-uniform TPMS channel whose frequencies are according to initial stress map (mid-left cols). Along with channel optimization, the interior channels optimize to distribute more materials in weak regions and less materials in strong regions (rightmost col).

6 DISCUSSION AND FUTURE WORK

We introduce a new 3D manufacturing approach of injecting the 3D shape with strong materials. For this purpose we utilize triply periodic minimal surfaces (TPMS) to define an inner channel structure that is smooth and connected. We use TPMS to define a channel structure inside the shape for injection of strong materials. After the object is 3D printed, we inject liquid materials through the TPMS, that once solidify yield strong support of the shape. Our strong TPMS allows injecting a wide range of materials in a fast and easy manner. Our results demonstrate the method's efficiency in terms of printing time and material as the object's interior is hollowed by TPMS channels.

In comparison with direct scaffolding methods, our method uses an implicit function to define the inner structure and therefore lacks a direct control over it. TPMS are however very simple in terms of their definition and application and present a significant progress over elaborate scaffolding techniques.

There might be alternatives for the TPMS channel to allow the injected fluid, such as the interior structures generated by topology optimization or some simple support structures. The essential requirements on the inner structures include connectivity, smoothness, free of dead-end,



Fig. 15. 3D printed models with TPMS channels inside. Some models are injected with blue epoxy resin. Some are left no injection for illustrating the channels.

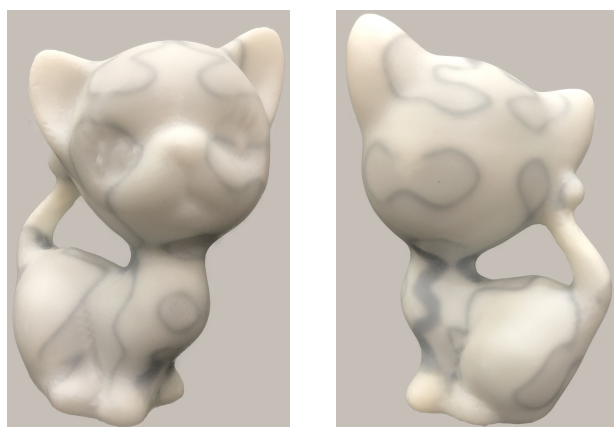


Fig. 16. The fabricated kitten model with CFRP injected.

and large surface-to-volume ratio. A smooth and connected tunnel allow the fluid to be injected from one entry hole, and to easily flow with no jam. Free of dead-end is also demanding, i.e., no local maximum exists along with the injecting, to guarantee no blocked air pocket inside the tunnel. Large surface-to-volume ratio indicates large contact area and thus helps the fluid to solidify quickly with efficient heat dissipation. As far as we know, interior structures driven by existing structural optimization methods can hardly satisfy all the requirements.

In the future, we would like to work on the analytic derivation of the optimization gradients and further explore our injection technique for a wider range of multiple material manufacturing. An immediate development is using TPMS channels in the context of elastic model design. Here we control the elasticity of a 3D printed object by injecting it with elastic material in a controlled manner. Similarly, we may follow our framework for exploring multi-material interaction. Thus, we control combinations of a wide range of materials through design of specific structures such as 3D one-, bi-directional nets and etc.

ACKNOWLEDGMENTS

We thank all the anonymous reviewers for their valuable comments and constructive suggestions. We thank Prof. Daniel Cohen-Or for his ideas and discussions. This work is supported by grants from National 973 Program (2015CB352501), NSFC (61572291), and Young Scholars Program of Shandong University (YSPSDU).

REFERENCES

- [1] L. Lu, A. Sharf, H. Zhao, Y. Wei, Q. Fan, X. Chen, Y. Savoye, C. Tu, D. Cohen-Or, and B. Chen, "Build-to-last: Strength to weight 3D printed objects," *ACM Trans. Graph.*, vol. 33, no. 4, pp. 97:1–97:10, Jul. 2014. [Online]. Available: <http://doi.acm.org/10.1145/2601097.2601168>
- [2] R. Hu, H. Li, H. Zhang, and D. Cohen-Or, "Approximate pyramidal shape decomposition," *ACM Trans. Graph.*, vol. 33, no. 6, pp. 213:1–213:12, Nov. 2014. [Online]. Available: <http://doi.acm.org/10.1145/2661229.2661244>
- [3] X. Chen, H. Zhang, J. Lin, R. Hu, L. Lu, Q. Huang, B. Benes, D. Cohen-Or, and B. Chen, "Dapper: Decompose-and-pack for 3D printing," *ACM Trans. Graph.*, vol. 34, no. 6, pp. 213:1–213:12, Oct. 2015. [Online]. Available: <http://doi.acm.org/10.1145/2816795.2818087>
- [4] H. Zhao, F. Gu, Q.-X. Huang, J. Garcia, Y. Chen, C. Tu, B. Benes, H. Zhang, D. Cohen-Or, and B. Chen, "Connected fermat spirals for layered fabrication," *ACM Trans. Graph.*, vol. 35, no. 4, pp. 100:1–100:10, Jul. 2016. [Online]. Available: <http://doi.acm.org/10.1145/2897824.2925958>
- [5] W. Wang, T. Y. Wang, Z. Yang, L. Liu, X. Tong, W. Tong, J. Deng, F. Chen, and X. Liu, "Cost-effective printing of 3D objects with skin-frame structures," *ACM Trans. Graph.*, vol. 32, no. 6, pp. 177:1–177:10, Nov. 2013. [Online]. Available: <http://doi.acm.org/10.1145/2508363.2508382>
- [6] X. Zhang, Y. Xia, J. Wang, Z. Yang, C. Tu, and W. Wang, "Medial axis tree - an internal supporting structure for 3D printing," *Comput. Aided Geom. Des.*, vol. 35, no. C, pp. 149–162, May 2015. [Online]. Available: <http://dx.doi.org/10.1016/j.cagd.2015.03.012>
- [7] O. Stava, J. Vanek, B. Benes, N. Carr, and R. M ech, "Stress relief: improving structural strength of 3D printable objects," *ACM Trans. Graph.*, vol. 31, no. 4, pp. 48:1–48:11, Jul. 2012.
- [8] S. Rajagopalan and R. A. Robb, "Schwarz meets schwann: Design and fabrication of biomorphic and duratoxic tissue engineering scaffolds," *Medical Image Analysis*, vol. 10, no. 5, pp. 693–712, 2006. [Online]. Available: <http://dx.doi.org/10.1016/j.media.2006.06.001>
- [9] F. P. Melchels, K. Bertoldi, R. Gabbriellini, A. H. Velders, J. Feijen, and D. W. Grijpma, "Mathematically defined tissue engineering scaffold architectures prepared by stereolithography," *Biomaterials*, vol. 31, no. 27, pp. 6909 – 6916, 2010. [Online]. Available: <http://www.sciencedirect.com/science/article/pii/S0142961210007210>

- [10] D.-J. Yoo, "Heterogeneous porous scaffold design for tissue engineering using triply periodic minimal surfaces," *International Journal of Precision Engineering and Manufacturing*, vol. 13, no. 4, pp. 527–537, Apr. 2012.
- [11] J. Shin, S. Kim, D. Jeong, H. G. Lee, D. Lee, J. Y. Lim, and J. Kim, "Finite element analysis of schwarz p surface pore geometries for tissue-engineered scaffolds," *Mathematical Problems in Engineering*, vol. 2012, p. 13, 2012. [Online]. Available: <http://dx.doi.org/10.1155/2012/694194>
- [12] A. H. Bermano, T. Funkhouser, and S. Rusinkiewicz, "State of the art in methods and representations for fabrication-aware design," *Computer Graphics Forum*, vol. 36, no. 2, pp. 509–535, 2017. [Online]. Available: <http://dx.doi.org/10.1111/cgf.13146>
- [13] M. Attene, M. Livesu, S. Lefebvre, T. Funkhouser, S. Rusinkiewicz, S. Ellero, J. Martinez, and A. H. Bermano, *Design, Representations, and Processing for Additive Manufacturing*. Morgan & Claypool Publishers, 2018.
- [14] S. Hollister, "Porous scaffold design for tissue engineering," *Nat. Mater.*, vol. 4, no. 7, pp. 518–524, 2005.
- [15] C. Schroeder, W. C. Regli, A. Shokoufandeh, and W. Sun, "Computer-aided design of porous artifacts," *Computer-Aided Design*, vol. 37, no. 3, pp. 339–353, 2005.
- [16] J. Kindinger, "Lightweight structural core," *ASM Handbook*, vol. 21, pp. 180–183, 2001.
- [17] S. Wilson, "Polymorphism of lipids," *Materials & Design*, vol. 11, no. 6, pp. 323–326, 1990.
- [18] Q. Zhou, J. Panetta, and D. Zorin, "Worst-case structural analysis," *ACM Trans. Graph.*, vol. 32, no. 4, pp. 137:1–137:12, Jul. 2013.
- [19] R. Prévost, E. Whiting, S. Lefebvre, and O. Sorkine-Hornung, "Make it stand: balancing shapes for 3D fabrication," *ACM Trans. Graph.*, vol. 32, no. 4, pp. 81:1–81:10, Jul. 2013.
- [20] X. Zhang, X. Le, Z. Wu, E. Whiting, and C. C. Wang, "Data-driven bending elasticity design by shell thickness," *Computer Graphics Forum*, vol. 35, no. 5, pp. 157–166, Aug. 2016. [Online]. Available: <https://doi.org/10.1111/cgf.12972>
- [21] P. Duysinx and M. P. Bendse, "Topology optimization of continuum structures with local stress constraints," *International Journal for Numerical Methods in Engineering*, vol. 43, no. 8, pp. 1453–1478, 1998. [Online]. Available: [https://doi.org/10.1002/\(SICI\)1097-0207\(19981230\)43:8%3C1453::AID-NME480%3E3.0.CO;2-2](https://doi.org/10.1002/(SICI)1097-0207(19981230)43:8%3C1453::AID-NME480%3E3.0.CO;2-2)
- [22] E. Holmberg, B. Torstenfelt, and A. Klarbring, "Stress constrained topology optimization," *Structural and Multidisciplinary Optimization*, vol. 48, no. 1, pp. 33–47, Jul. 2013. [Online]. Available: <https://doi.org/10.1007/s00158-012-0880-7>
- [23] J. Wu, C. Dick, and R. Westermann, "A system for high-resolution topology optimization," *IEEE Transactions on Visualization and Computer Graphics*, vol. 22, no. 3, pp. 1195–1208, March 2016.
- [24] J. Liu and Y. Ma, "A survey of manufacturing oriented topology optimization methods," *Advances in Engineering Software*, vol. 100, pp. 161–175, 2016. [Online]. Available: <http://www.sciencedirect.com/science/article/pii/S0965997816302174>
- [25] J. Liu, A. T. Gaynor, S. Chen, Z. Kang, K. Suresh, A. Takezawa, L. Li, J. Kato, J. Tang, C. C. L. Wang, L. Cheng, X. Liang, and A. C. To, "Current and future trends in topology optimization for additive manufacturing," *Structural and Multidisciplinary Optimization*, May 2018. [Online]. Available: <https://doi.org/10.1007/s00158-018-1994-3>
- [26] J. Wu, N. Aage, R. Westermann, and O. Sigmund, "Infill optimization for additive manufacturing - approaching bone-like porous structures," *IEEE Transactions on Visualization and Computer Graphics*, vol. 24, no. 2, pp. 1127–1140, Feb. 2018.
- [27] J. Wu, C. C. Wang, X. Zhang, and R. Westermann, "Self-supporting rhombic infill structures for additive manufacturing," *Computer-Aided Design*, vol. 80, no. Supplement C, pp. 32–42, 2016. [Online]. Available: <http://www.sciencedirect.com/science/article/pii/S0010448516300690>
- [28] U. Dierkes, S. Hildebrandt, and F. Sauvigny, *Minimal Surfaces*. Berlin, Heidelberg: Springer Berlin Heidelberg, 2010, pp. 53–90. [Online]. Available: https://doi.org/10.1007/978-3-642-11698-8_2
- [29] O. Busaryev, T. K. Dey, H. Wang, and Z. Ren, "Animating bubble interactions in a liquid foam," *ACM Trans. Graph.*, vol. 31, no. 4, pp. 63:1–63:8, Jul. 2012.
- [30] F. Da, C. Batty, C. Wojtan, and E. Grinspun, "Double bubbles sans toil and trouble: Discrete circulation-preserving vortex sheets for soap films and foams," *ACM Trans. Graph.*, vol. 34, no. 4, pp. 149:1–149:9, Jul. 2015.
- [31] J. Pérez, M. A. Otaduy, and B. Thomaszewski, "Computational design and automated fabrication of kirchhoff-plateau surfaces," *ACM Trans. Graph.*, vol. 36, no. 4, pp. 62:1–62:12, Jul. 2017. [Online]. Available: <http://doi.acm.org/10.1145/3072959.3073695>
- [32] A. Schoen, *Infinite Periodic Minimal Surfaces Without Self-intersections*, ser. NASA TN D. National Aeronautics and Space Administration, 1970. [Online]. Available: https://books.google.co.il/books?id=LxOb_NIMLmC
- [33] D. Cvijovi and J. Klinowski, "The T and CLP families of triply periodic minimal surfaces," *Journal De Physique*, vol. 2, no. 12, pp. 2191–2205, 1992.
- [34] L. Han and S. Che, "An overview of materials with triply periodic minimal surfaces and related geometry: From biological structures to self-assembled systems," *Advanced Materials*, vol. 30, no. 17, p. 1705708, 2018. [Online]. Available: <https://onlinelibrary.wiley.com/doi/abs/10.1002/adma.201705708>
- [35] S. Khaderi, V. Deshpande, and N. Fleck, "The stiffness and strength of the gyroid lattice," *International Journal of Solids and Structures*, vol. 51, no. 23, pp. 3866–3877, 2014. [Online]. Available: <http://www.sciencedirect.com/science/article/pii/S002076831400256X>
- [36] Z. Qin, G. S. Jung, M. J. Kang, and M. J. Buehler, "The mechanics and design of a lightweight three-dimensional graphene assembly," *Science Advances*, vol. 3, no. 1, p. e1601536, Jan. 2017. [Online]. Available: <http://www.ncbi.nlm.nih.gov/pmc/articles/PMC5218516/>
- [37] L. Zhang, S. Feih, S. Daynes, S. Chang, M. Y. Wang, J. Wei, and W. F. Lu, "Energy absorption characteristics of metallic triply periodic minimal surface sheet structures under compressive loading," *Additive Manufacturing*, 2018. [Online]. Available: <http://www.sciencedirect.com/science/article/pii/S2214860418304688>
- [38] D. Li, W. Liao, N. Dai, G. Dong, Y. Tang, and Y. M. Xie, "Optimal design and modeling of gyroid-based functionally graded cellular structures for additive manufacturing," *Computer-Aided Design*, vol. 104, pp. 87–99, 2018. [Online]. Available: <http://www.sciencedirect.com/science/article/pii/S0010448518300381>
- [39] J. Panetta, Q. Zhou, L. Malomo, N. Pietroni, P. Cignoni, and D. Zorin, "Elastic textures for additive fabrication," *ACM Trans. Graph.*, vol. 34, no. 4, pp. 135:1–135:12, Jul. 2015. [Online]. Available: <http://doi.acm.org/10.1145/2766937>
- [40] C. Schumacher, B. Bickel, J. Rys, S. Marschner, C. Daraio, and M. Gross, "Microstructures to control elasticity in 3D printing," *ACM Trans. Graph.*, vol. 34, no. 4, pp. 136:1–136:13, Jul. 2015. [Online]. Available: <http://doi.acm.org/10.1145/2766926>
- [41] J. Martínez, J. Dumas, and S. Lefebvre, "Procedural voronoi foams for additive manufacturing," *ACM Trans. Graph.*, vol. 35, no. 4, pp. 44:1–44:12, Jul. 2016. [Online]. Available: <http://doi.acm.org/10.1145/2897824.2925922>
- [42] J. Martínez, H. Song, J. Dumas, and S. Lefebvre, "Orthotropic k-nearest foams for additive manufacturing," *ACM Trans. Graph.*, vol. 36, no. 4, pp. 121:1–121:12, Jul. 2017. [Online]. Available: <http://doi.acm.org/10.1145/3072959.3073638>
- [43] J. Martínez, S. Hornus, H. Song, and S. Lefebvre, "Polyhedral voronoi diagrams for additive manufacturing," *ACM Trans. Graph.*, vol. 37, no. 4, pp. 129:1–129:15, Jul. 2018. [Online]. Available: <http://doi.acm.org/10.1145/3197517.3201343>
- [44] J. Panetta, A. Rahimian, and D. Zorin, "Worst-case stress relief for microstructures," *ACM Trans. Graph.*, vol. 36, no. 4, pp. 122:1–122:16, Jul. 2017. [Online]. Available: <http://doi.acm.org/10.1145/3072959.3073649>
- [45] K. Vidimče, S.-P. Wang, J. Ragan-Kelley, and W. Matusik, "Openfab: A programmable pipeline for multi-material fabrication," *ACM Trans. Graph.*, vol. 32, no. 4, pp. 136:1–136:12, Jul. 2013. [Online]. Available: <http://doi.acm.org/10.1145/2461912.2461993>
- [46] K. Vidimce, A. Kaspar, Y. Wang, and W. Matusik, "Foundry: Hierarchical material design for multi-material fabrication," in *Proceedings of the 29th Annual Symposium on User Interface Software and Technology*, ser. UIST '16. New York, NY, USA: ACM, 2016, pp. 563–574. [Online]. Available: <http://doi.acm.org/10.1145/2984511.2984516>
- [47] M. Skouras, B. Thomaszewski, S. Coros, B. Bickel, and M. Gross, "Computational design of actuated deformable characters," *ACM Trans. Graph.*, vol. 32, no. 4, pp. 82:1–82:10, Jul. 2013. [Online]. Available: <http://doi.acm.org/10.1145/2461912.2461979>
- [48] L.-K. Ma, Y. Zhang, Y. Liu, K. Zhou, and X. Tong, "Computational design and fabrication of soft pneumatic

objects with desired deformations," *ACM Trans. Graph.*, vol. 36, no. 6, pp. 239:1–239:12, Nov. 2017. [Online]. Available: <http://doi.acm.org/10.1145/3130800.3130850>

- [49] J. Zehnder, E. Knoop, M. Bäcker, and B. Thomaszewski, "Metasilicone: Design and fabrication of composite silicone with desired mechanical properties," *ACM Trans. Graph.*, vol. 36, no. 6, pp. 240:1–240:13, Nov. 2017. [Online]. Available: <http://doi.acm.org/10.1145/3130800.3130881>
- [50] H. Nance, <https://makezine.com/2014/04/24/stress-testing-injected-hot-glue-for-solid-fast-cheap-3d-prints/>, Apr. 2014. [Online]. Available: <https://makezine.com/2014/04/24/stress-testing-injected-hot-glue-for-solid-fast-cheap-3d-prints/>
- [51] L. Malomo, N. Pietroni, B. Bickel, and P. Cignoni, "Flexmolds: Automatic design of flexible shells for molding," *ACM Trans. Graph.*, vol. 35, no. 6, pp. 223:1–223:12, Nov. 2016. [Online]. Available: <http://doi.acm.org/10.1145/2980179.2982397>
- [52] K. Nakashima, T. Auzinger, E. Iarussi, R. Zhang, T. Igarashi, and B. Bickel, "Corecavity: Interactive shell decomposition for fabrication with two-piece rigid molds," *ACM Trans. Graph.*, vol. 37, no. 4, pp. 135:1–135:13, Jul. 2018. [Online]. Available: <http://doi.acm.org/10.1145/3197517.3201341>
- [53] T. Alderighi, L. Malomo, D. Giorgi, N. Pietroni, B. Bickel, and P. Cignoni, "Metamolds: Computational design of silicone molds," *ACM Trans. Graph.*, vol. 37, no. 4, pp. 136:1–136:13, Jul. 2018. [Online]. Available: <http://doi.acm.org/10.1145/3197517.3201381>
- [54] Y. Jung and S. Torquato, "Fluid permeabilities of triply periodic minimal surfaces," *Phys. Rev. E*, vol. 72, p. 056319, Nov 2005. [Online]. Available: <https://link.aps.org/doi/10.1103/PhysRevE.72.056319>
- [55] V. J. Challis, J. K. Guest, J. F. Grotowski, and A. P. Roberts, "Computationally generated cross-property bounds for stiffness and fluid permeability using topology optimization," *International Journal of Solids and Structures*, vol. 49, no. 23, pp. 3397 – 3408, 2012. [Online]. Available: <http://www.sciencedirect.com/science/article/pii/S0020768312003204>
- [56] A. M. Mirzendehtdel and K. Suresh, "Support structure constrained topology optimization for additive manufacturing," *Computer-Aided Design*, vol. 81, pp. 1 – 13, 2016. [Online]. Available: <http://www.sciencedirect.com/science/article/pii/S0010448516300951>
- [57] B. Patzák, "OOFEM - an object-oriented simulation tool for advanced modeling of materials and structures," *Acta Polytechnica*, vol. 52, no. 6, pp. 59–66, 2012.
- [58] Wikipedia, "Carbon fiber reinforced polymer," 2018. [Online]. Available: https://en.wikipedia.org/wiki/Carbon_fiber_reinforced_polymer



Lin Lu is an Associate Professor in School of Computer Science and Technology, Shandong University (SDU). She received the B.Eng. and M.Eng. degree in School of Computer Science and Technology at Shandong University in 2002 and 2005, respectively. She completed her Ph.D. degree in the Graphics Group led by Prof. Wenping Wang at The University of Hong Kong in 2011. Her current research focuses on geometric modeling and creative design for digital fabrication.



Andrei Sharf is an Associate Professor at the Computer Science Department, Ben-Gurion University. Previous to that he was a Visiting Associate Professor at the Shenzhen Institute of Advanced Technology (SIAT) China. He did his PostDoc with Prof. Nina Amenta at the Institute for Data Analysis and Visualization (IDAV), University of California at Davis. His PhD was carried under the supervision of Prof. Daniel Cohen-Or and Prof. Ariel Shamir at the School of Computer Science, Tel-Aviv University. His research is in the realm of Computer Graphics, concentrating on geometry processing and 3D modeling. A major part of his research focuses on techniques and algorithms for 3D scanning and point processing (reconstruction, understanding, etc.).



Haisen Zhao received M.Eng. and B.Eng. degree in School of Computer Science and Technology and School of Software at Shandong University in 2014 and 2011, respectively. After then he received his Ph.D degree in the School of Computer Science and Technology at Shandong University in 2018, supervised by Prof. Baoquan Chen. His research interests include computer graphics and intelligent manufacture.



Xin Yan received the B.Eng. and M.Eng. degree in School of Mechanical Engineering at Shandong University in 2014 and 2017, respectively. He is currently a Ph.D candidate in the School of Computer Science and Technology at Shandong University, supervised by Dr. Lin Lu. His research interests include geometric modeling in the field of Computer Graphics.



Cong Rao received the B.Eng. degree in School of Computer Science and Technology at Shandong University in 2017. He is currently a master student in the School of Computer Science and Technology at Shandong University, supervised by Dr. Lin Lu. His research interests include geometric modeling in the field of Computer Graphics.



Baoquan Chen is a Professor of Peking University, where he is the Executive Director of the Center on Frontiers of Computing Studies. Prior to the current post, he was the Dean of School of Computer Science and Technology at Shandong University, and the founding director of the Visual Computing Research Center, Shenzhen Institute of Advanced Technology (SIAT), Chinese Academy of Sciences (2008-2013), and a faculty member at Computer Science and Engineering at the University of Minnesota at Twin Cities (2000-2008). His research interests generally lie in computer graphics, visualization, and human-computer interaction, focusing specifically on large-scale city modeling, simulation and visualization. He has published more than 100 papers in international journals and conferences, including two dozens or so papers in SIGGRAPH and SIGGRAPH Asia. Chen received an MS in Electronic Engineering from Tsinghua University, Beijing (1994), and a second MS (1997) and then PhD (1999) in Computer Science from the State University of New York at Stony Brook. Chen is the recipient of the Microsoft Innovation Excellence Program 2002, the NSF CAREER award 2003, McKnight Land-Grant Professorship for 2004, IEEE Visualization Best Paper Award 2005, and NSFC "Outstanding Young Researcher" program in 2010. Chen served as conference co-chair of IEEE Visualization 2005, and served as the conference chair of SIGGRAPH Asia 2014.

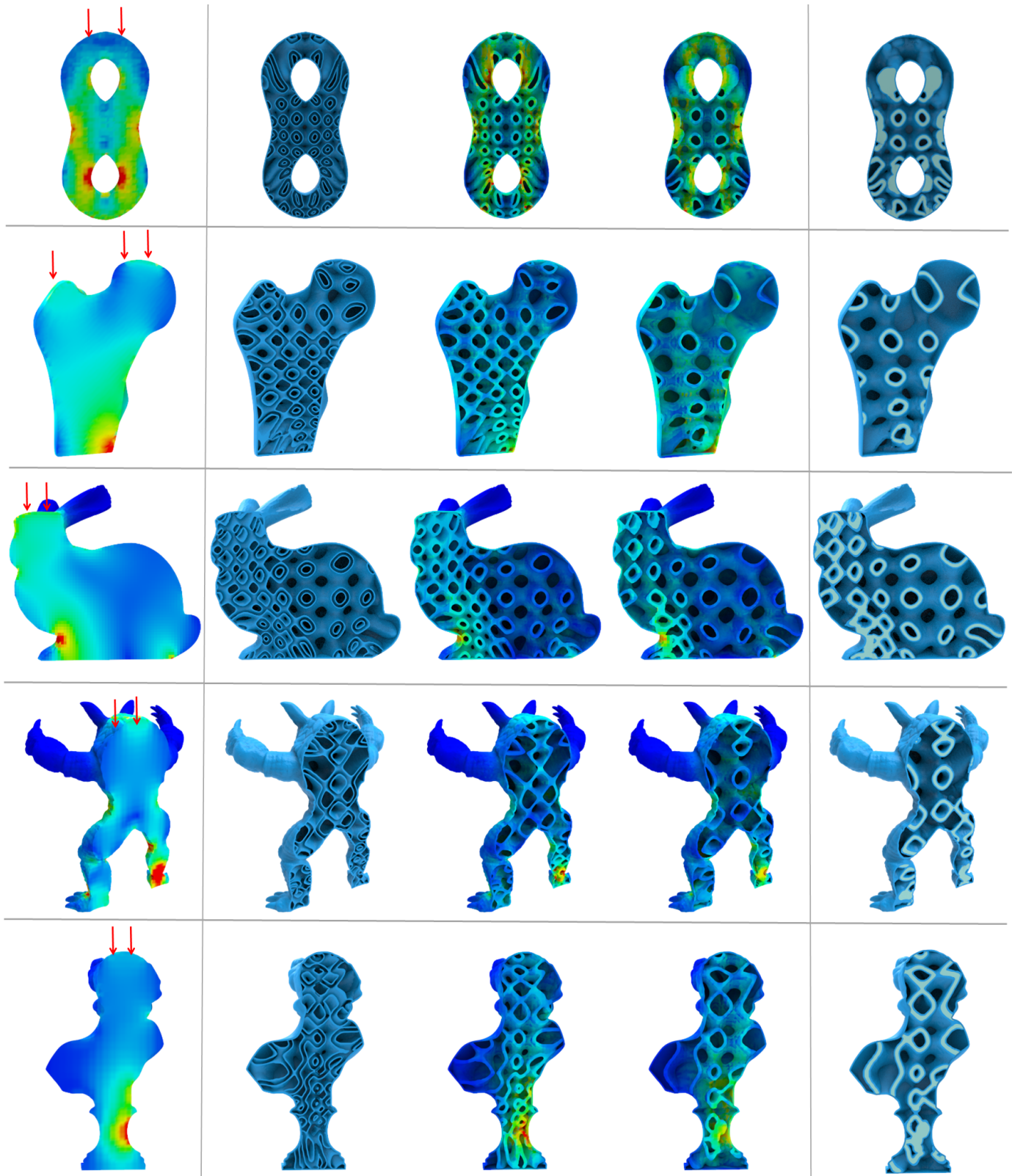


Fig. 17. TPMS channel optimization results for five models (rows). Left-to-right columns, original model with initial stress map, initial TPMS channel, initial TPMS channel with stresses, optimized TPMS channel with stresses, and optimized TPMS channel with injected fluid.